Journal of Fluids and Structures (2002) **16**(4) 543–560
doi:10.1006/jfls.2001.0436 available online at http://www.idealibrary.com on IDEAL®

A THEORETICAL STUDY OF PAPER FLUTTER

Y. Watanabe
Ryoken Tech Co., Ltd., Nagasaki, Japan

K. Isogai
Department of Aeronautics and Astronautics, Kyushu University, Fukuoka, Japan
and
S. Suzuki and M. Sugihara
Hiroshima Research & Development Center, Mitsubishi Heavy Ind., Ltd. Mihara, Japan

(Received 30 June 2000, and in final form 11 September 2001)

Two different methods of analysis were developed in order to clarify the phenomenon of paper flutter. One of these is a flutter simulation using a Navier–Stokes code (N–S simulation). N–S simulation was used to determine the unsteady lift force, the amplitude of flutter, and the air-flow around a paper sheet, by means of a time-marching scheme. The other form of analysis is based on a potential-flow analysis of an oscillating thin airfoil via an eigenvalue analysis for determining stability. The flutter speeds and flutter modes obtained by each method are consistent. Aspects of the behavior of paper flutter that had not been clarified in the experimental analysis were clarified by potential flow analysis. From the results of this study, it was shown that potential flow analysis is very convenient and adequate for a parametric study of this problem.

1. INTRODUCTION

Experimental and numerical studies have been carried out since around 1990 for the purpose of clarifying the paper flutter phenomenon, which currently limits the speed of printing machines and paper machines; see, e.g., Watanabe *et al.* (1991, 1997). The findings of these studies are presented in two papers. The first paper (Watanabe *et al.* 2002) describes the background of the study and the conditions of paper flutter in real machinery, and reported on the experimental study in which wind tunnel tests were conducted. This, the second paper, reports on the theoretical study, in which two numerical methods using a super-computer and a personal computer were employed.

First, we present the features of each of the present methods and the relationship with other recently reported methods. The theoretical study of the sheet flutter phenomenon can be classified, as shown in Table 1, according to the analysis domain (time or frequency), the flow field, and the stability analysis used. These methods are all two-dimensional; the cost and time required for a three-dimensional analysis of this problem are prohibitive, and it is considered that in most circumstances, flutter behaviour can be well approximated by a two-dimensional model. The methods of analysis in the present study are listed as items 3 and 7 in Table 1.

0889-9746/02/040543 + 18 $35.00/0

TABLE 1
Various methods for sheet flutter analysis

Method	Analysis domain	Flow field	Stability analysis	References
1	Time domain	Potential flow	Energy analysis by assumed-mode method	Noguchi *et al.* (1995)
2	Time domain	Potential flow	Time-marching analysis by generalized coordinate	Huang (1995)
3	Time domain	Viscous flow	Time-marching analysis by Navier-Stokes code	Present study
4	Frequency domain	Potential flow	Eigenvalue analysis by 300th-order determinant for multi-elements	Yamaguchi *et al.* (1999)
5	Frequency domain	Potential flow	Eigenvalue analysis second-order determinant for generalized coordinates	Kornecki *et al.* (1976)
6	Frequency domain	Potential flow	Eigenvalue analysis by 10th-order determinant for generalized coordinates	Guo & Païdoussis (2000)
7	Frequency domain	Potential flow	Eigenvalue analysis by fourth-order determinant for generalized coordinates ($U-g$ method)	Present study

Method 1 was adopted by Noguchi *et al.* (1995), in which the unsteady lift for an assumed mode was analysed by the vortex method, and instability was determined from the change in energy of the sheet, induced by unsteady lift. It is difficult to accurately estimate flutter conditions with an assumed mode, because the flutter mode of a sheet is not simple. Method 2 was adopted by Huang (1995), in which the unsteady lift was determined by potential flow theory, and the response was analysed in the form of a time-marching scheme by solving the equations of motion for the generalized coordinates. A stability boundary was determined from the growth exponent.

Method 3 is the first method employed in the present study, in which the unsteady lift, the response of the paper sheet, and the flow around the sheet were numerically analysed by Navier–Stokes code with a time-marching solution; see, Isogai (1993). The stability boundary was determined from the growth exponent in the same manner as method 2. A super-computer was used to conduct the N–S simulation of method 3, and the computation time was up to several hours for a single case. Method 4 was adopted by Yamaguchi *et al.* (1999), in which the chord of a paper sheet was divided into 50 elements, with 306 equations $[(50+1)\times(6 \text{ unknown variables})=306]$. Stability was determined using a high-order (300) determinant. Method 5 by Kronecki *et al.* (1976), method 6 by Guo & Païdoussis (2000) and method 7 in the present study are all based on an eigenvalue analysis for the generalized coordinates. However, the methods differ in several ways. The flutter determinant was obtained using Galerkin's method in methods 5 and 6, whereas here it is obtained by applying Lagrange's equation. Furthermore, second- and 10th-order flutter determinants were used in methods 5 and 6, while here we employ a fourth-order determinant; the effective range of the solution using the second-order determinant is limited to a region of high mass ratio, and the 10th-order determinant appears excessive. Method 7 appears to be the most convenient of the existing methods.

In this paper, the details of the applications of methods 3 and 7, and the behaviour of sheet flutter as described by these methods, are reported.

2. EQUATIONS OF MOTION

The displacement y of the sheet can be represented by the series:

$$y(x,\ t) = \sum_{i=1}^{n} q_i(t) f_i(x), \tag{1}$$

where $q_i(t)$ are the generalized coordinates and $f_i(x)$ are the natural modes. The modes of a cantilever beam were used for $f_i(x)$,

$$f_i(x) = \tfrac{1}{2}[\{\cosh(R_i\, x/c) - \cos(R_i\, x/c)\} - S_i\{\sinh(R_i\, x/c) - \sin(R_i\, x/c)\}], \tag{2}$$

where the values of R_i and S_i for $i = 1-4$ are as follows:

$$R_1 = 1{\cdot}875,\ R_2 = 4{\cdot}694,\ R_3 = 7{\cdot}855,\ R_4 = 19{\cdot}996,$$
$$S_1 = 0{\cdot}734,\ S_2 = 1{\cdot}018,\ S_3 = 1{\cdot}000,\ S_4 = 1{\cdot}000.$$

The equations of motion for q_i can be derived using Lagrange's equation, [see, e.g., Bisplinghoff *et al.* (1955)], as follows:

$$M_i \ddot{q}_i + \omega_i^2 M_i q_i = Q_{Li} + Q_{Di}, \tag{3}$$

where M_i is the generalized mass of the paper sheet, and can be written for each mode of cantilever beam as

$$M_i = m \int_{-b}^{b} f_i^2 \,\mathrm{d}x = mc/4; \tag{4}$$

Q_{Li} is the generalized lift due to the unsteady lift, and Q_{Di} is the generalized drag due to the y-direction component of friction drag acting along the sheet surface. Q_{Li} and Q_{Di} are expressed as

$$Q_{Li} = \int_{-b}^{b} p(x,\ t) f_i \,\mathrm{d}x, \tag{5}$$

$$Q_{Di} = \int_{-b}^{b} \left\{ \frac{\mathrm{d}}{\mathrm{d}x} T(x) \frac{\mathrm{d}y}{\mathrm{d}x} \right\} f_i \,\mathrm{d}x = \frac{1}{2} \rho U^2 C_D \int_{-b}^{b} \left\{ \frac{\mathrm{d}}{\mathrm{d}x} (b - x) \frac{\mathrm{d}y}{\mathrm{d}x} \right\} f_i \,\mathrm{d}x, \tag{6}$$

where $T(x)$ is the tension due to the friction drag. The equations of motion are analyzed using the N–S simulation and the potential flow analysis in order to obtain the flutter speeds of paper sheets, as described in the following. Tension was not introduced in the N–S simulation.

3. NAVIER–STOKES SIMULATION

3.1. Simulation Method

The Navier–Stokes (N–S) simulation method is outlined in Figure 1. The computational code applied to the analysis of unsteady lift is a 2-D compressible N–S code. This code was originally developed for the simulation of dynamic stall phenomenon for an airfoil oscillating near the static stall angle. For analysis in the incompressible regime, a good correlation with experiments has been obtained at a low Mach number, $M = 0{\cdot}3$.

The Yee–Harten TVD Scheme (Yee & Harten 1985) was employed as the finite difference technique to solve the N–S equations. The grid used for the calculation is a body-fitted grid that moves with the motion of the sheet. The equations of motion for the generalized coordinates were then analysed using Houbolt's method (Houbolt 1950) for

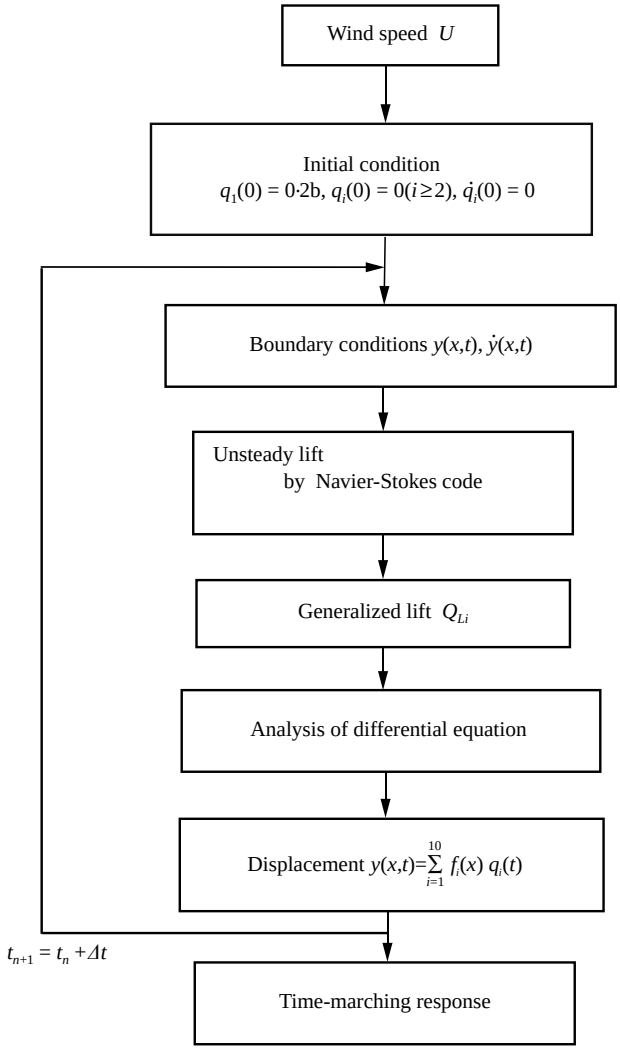

Figure 1. Flutter simulation by Navier–Stokes code (N–S simulation).

the finite difference equations. The analysis is iterated until the rate of growth or damping can be determined. The conditions of analysis are as follows: (i) properties of the sheet: $c = 0{\cdot}297\,\text{m}$, $h = 106\,\mu\text{m}$, $\rho_p = 1340\,\text{kg/m}^3$, $E = 3{\cdot}23 \times 10^9\,\text{Pa}$, (ii) mass ratio: $\mu = 0{\cdot}39$, (iii) number of natural modes: 10, (iv) dimensionless time step: $\Delta t(U/b) = 6 \times 10^{-4}$.

3.2. Response and Flutter Speed of Paper Sheet

The responses of modes 1–4 in the unstable region ($U = 1{\cdot}6\,\text{m/s}$) in the N–S simulation are shown in Figure 2(a). The frequencies of all modes are consistent after half a cycle from the start of the calculation. The amplitudes can be seen to grow with time. The first mode exhibits the largest amplitude, and the amplitude decreases in the second, third and

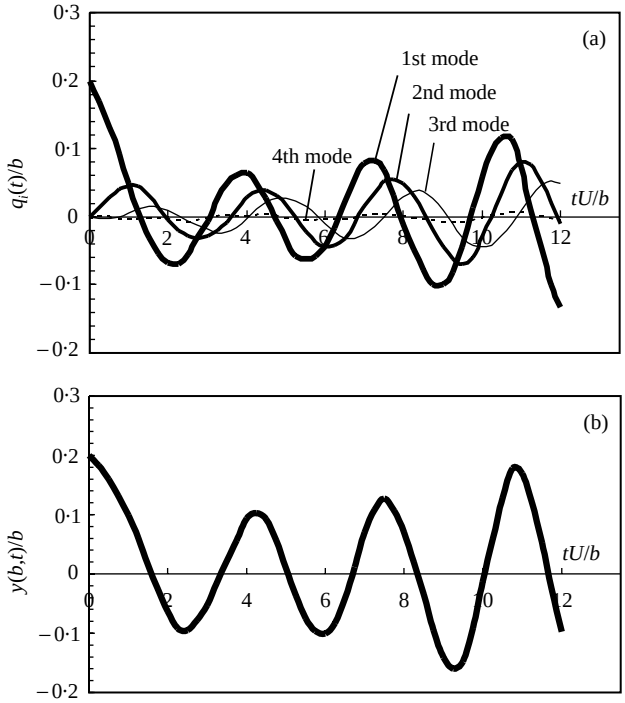

Figure 2. Time-marching response by N–S simulation, in the unstable region ($U = 1 \cdot 6$ m/s, $\mu = 0 \cdot 39$): (a) response of the component mode; (b) response of the trailing edge.

fourth mode, in that order. The amplitudes of the fifth and higher modes are small enough to be ignored. The flutter frequency is $3 \cdot 26$ Hz. In this case, the natural frequency of the third mode ($5 \cdot 26$ Hz) was lowered by the unsteady lift, to the value obtained for the flutter frequency. The overall response of the trailing-edge of the sheet, shown in Figure 2(b), was obtained by superposing the amplitudes of each mode $q_i(t)$ in Figure 2(a). The time history is similar to that of the first mode, $q_1(t)$.

The amplitude can be seen to be most influenced by the first mode, and the frequency to be most affected by the natural frequency of the third mode. Figure 3 shows the response of the sheet in the stable region ($U = 1 \cdot 3$ m/s). The flutter speed was defined as the wind speed at which the growth exponent becomes zero. Thus, the flutter speed is $1 \cdot 46$ m/s from the positive exponent of Figure 2(b) and the negative exponent of Figure 3(b). The dimensionless flutter speed is defined by the following formula:

$$U_S^* = U_S/(EI/\rho c^3)^{1/2}. \tag{7}$$

The dimensionless flutter speed was calculated to be $14 \cdot 6$. This result is used to verify the accuracy of the potential flow analysis.

3.3. Flow around Sheet

Figure 4(a) shows the isovorticity contours of the airflow around a deformed sheet at rest as generated by N–S simulation. Figure 4(b) shows the same simulation results for a

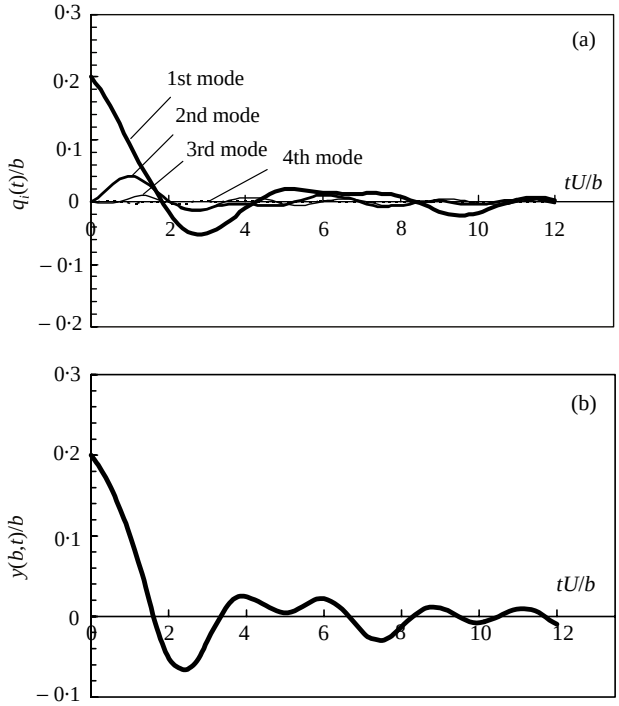

Figure 3. Time-marching response by N–S simulation, in the stable region ($U = 1{\cdot}3\,\mathrm{m/s}$, $\mu = 0{\cdot}39$): (a) response of the component mode (b) response of the trailing edge.

fluttering sheet. Large-scale air-flow separation was observed in the deformed sheet at rest, and yet no separation was observed in the fluttering sheet, in spite of the large-scale movement. Figure 4(c) shows the air-flow around the fluttering sheet from wind tunnel tests (Watanabe *et al*. 2002), using the smoke-wire method. The air-flow behaviour in the simulation is consistent with that observed in this experiment. The air-flow in both cases is close to that obtained by the potential flow theory. From these results, potential flow theory is considered to be applicable to the analysis of sheet flutter.

4. POTENTIAL FLOW ANALYSIS

4.1. Method of Analysis

Potential flow analysis in the frequency domain was carried out by using the four natural beam modes, as it was shown by the N–S simulation that modes higher than the fifth could be ignored in flutter analysis. The method of potential flow analysis is outlined in Figure 5. Aerodynamic analysis involves the analysis of the generalized unsteady lift Q_{Lij} of the $4 \times 4 = 16$ element system using the theory of an oscillating thin airfoil in inviscid incompressible flow. The unsteady lift, once calculated, can be used universally for flutter analysis in all conditions. Stability analysis involves the eigenvalue analysis of a 4×4 determinant, and at the same time, the flutter speed, frequency and mode are obtained.

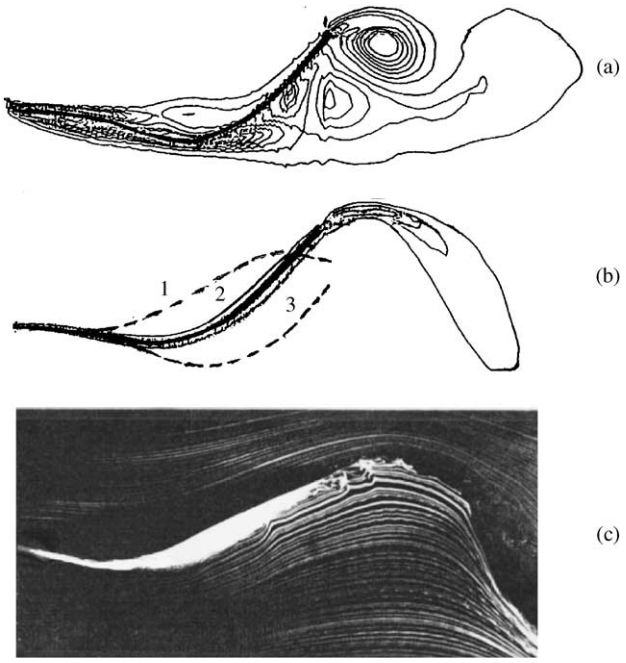

Figure 4. Flow around sheet: (a) isovorticity contour around a deformed sheet at rest by N–S simulation ; (b) isovorticity contour around a fluttering sheet by N–S simulation (the sheet moves from 1 for 3); (c) streamlines around a fluttering sheet by smoke-wire test.

4.2. Analysis of Aerodynamic Force

4.2.1. Generalized force due to unsteady lift

The unsteady pressure of a sheet that oscillates in simple harmonic motion in the jth mode is expressed as follows:

$$p_j(\theta) = \frac{1}{2}\rho U^2 c_{pj}(\theta)/b, \tag{8}$$

where $c_{pj}(\theta, t)$ is the pressure coefficient, which can be expressed as follows according to the Küssner–Schwarz (1941) theory:

$$c_{pj}(\theta) = \frac{4}{\pi}\int_0^{\pi}\left(\mathrm{i}kf_j + b\frac{\mathrm{d}f_j}{\mathrm{d}x}\right)\left[\{C(k)(1-\cos\theta^*)+\cos\theta^*\}\cot\frac{\theta}{2}\right.$$
$$\left.+\mathrm{i}k\frac{1}{2}\ln\frac{1-\cos(\theta+\theta^*)}{1-\cos(\theta-\theta^*)}\sin\theta - \sin\theta^*\frac{\sin\theta}{\cos\theta^*-\cos\theta}\right]\mathrm{d}\theta^*,$$

where $C(k)$ is Theodorsen's function. The following approximation (Fung 1955) was used in the present analysis:

$$C(k) = 1 - \frac{0{\cdot}165}{1-(0{\cdot}041/k)\mathrm{i}} - \frac{0{\cdot}335}{1-(0{\cdot}32/k)\mathrm{i}}. \tag{10}$$

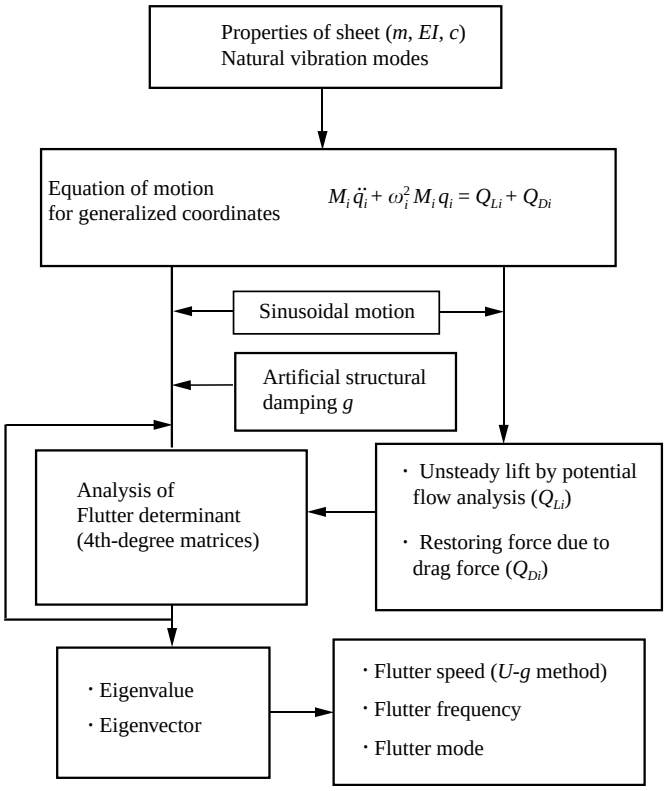

Figure 5. Flutter simulation by potential flow analysis.

From equations (5) and (8), Q_{Li} is

$$Q_{Li} = \sum_{j=1}^{4} \int_b^b p_j(\theta,\, t) f_i \,\mathrm{d}x = \frac{1}{2}\rho U^2 \sum_{j=1}^{4} \left\{ \int_0^{\pi} c_{pj}(\theta) f_i \sin\theta \,\mathrm{d}\theta \right\} q_j$$
$$= \frac{1}{2}\rho U^2 \sum_{j=1}^{4} C_{Lij} q_j, \tag{11}$$

where

$$C_{Lij} = \int_0^{\pi} c_{pj}(\theta) f_i \sin\theta \,\mathrm{d}\theta. \tag{12}$$

Since C_{Lij} is a complex number, it is represented in the complex form by

$$C_{Lij} = C_{LijR} + \mathrm{i}C_{LijI} \tag{13}$$

where C_{LijR} and C_{LijI} are the real and imaginary parts of C_{Lij}. The 16 elements of C_{LijR} and C_{LijI} are calculated using equations (8)–(13), and shown in Figures 6 and 7.

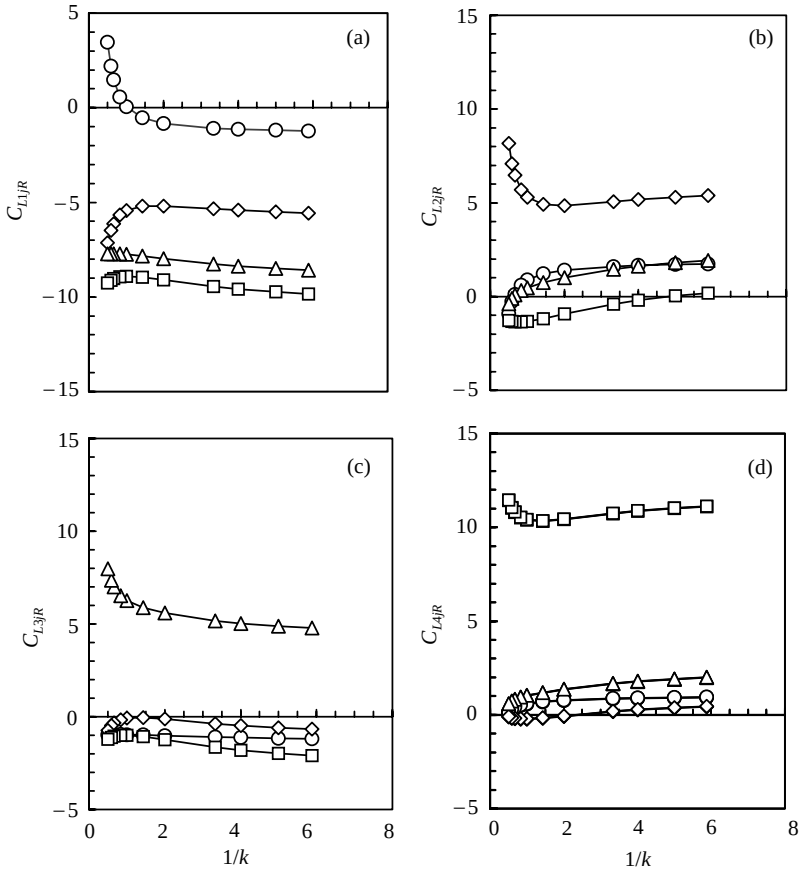

Figure 6. Unsteady lift coefficients (Real part): ○, j = 1;◇, j = 2; △, j = 3; □, j = 4. (a) Lift by first mode motion; (b) second mode motion; (c) third mode motion; (d) fourth mode motion.

4.2.2. Generalized force due to aerodynamic drag

By applying integration by parts to equation (6), Q_{Di} can be expressed as

$$Q_{Di} = \frac{1}{2}\rho U^2 C_D \sum_{j=1}^{n} \int_{-b}^{b} f_i \left\{ \frac{\mathrm{d}}{\mathrm{d}x}\left((b-x)\frac{\mathrm{d}f_j}{\mathrm{d}x} \right) \right\} \mathrm{d}x\, q_j$$

$$= -\frac{1}{2}\rho U^2 C_D \sum_{j=1}^{n} \int_{-1}^{1} (1-x^*)\frac{\mathrm{d}f_i}{\mathrm{d}x^*}\frac{\mathrm{d}f_j}{\mathrm{d}x^*}\mathrm{d}x^* q_j = -\frac{1}{2}\rho U^2 \sum_{j=1}^{n} C_{Dij} q_j, \qquad (14)$$

where

$$C_{Dij} = C_D \int_{-1}^{1} (1-x^*)\frac{\mathrm{d}f_i}{\mathrm{d}x^*}\frac{\mathrm{d}f_j}{\mathrm{d}x^*}\mathrm{d}x^*. \qquad (15)$$

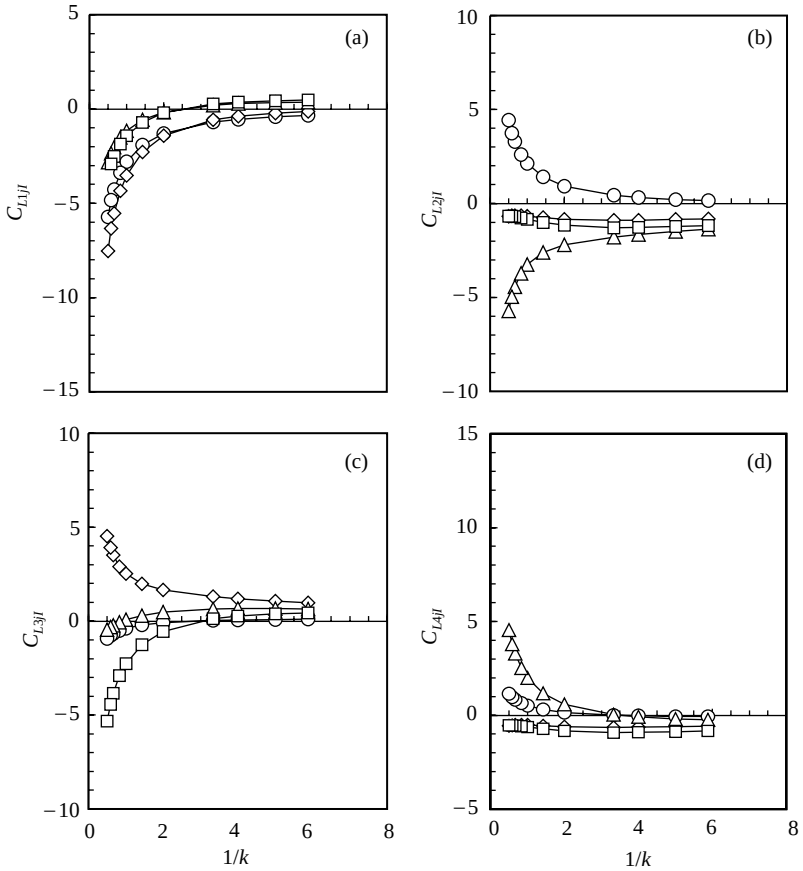

Figure 7. Unsteady lift coefficients (imaginary part): ○, j = 1; ◇, j = 2; △, j = 3; □, j = 4. (a) Lift by first mode motion; (b) second mode motion; (c) third mode motion; (d) fourth mode motion.

4.3. Flutter Determinant

By substituting equations (11) and (14) into equation (3), the equation of motion becomes

$$M_i\ddot{q}_i + \omega_i^2 M_i q_i = \frac{1}{2}\rho U^2 \sum_{j=1}^{4} C_{Lij} q_j - \frac{1}{2}\rho U^2 \sum_{j=1}^{4} C_{Dij} q_j, \quad i = 1{-}4. \tag{16}$$

By assuming that the flutter motion is harmonic, and by introducing artificial damping, g, which is necessary to maintain sinusoidal motion, the following flutter determinant can be derived:

$$\begin{vmatrix} Z - A_{11} & -A_{12} & -A_{13} & -A_{14} \\ -A_{21} & \Omega_2 Z - A_{22} & -A_{23} & -A_{24} \\ -A_{31} & -A_{32} & \Omega_3 Z - A_{33} & -A_{34} \\ -A_{41} & -A_{42} & -A_{43} & \Omega_4 Z - A_{44} \end{vmatrix} = 0, \tag{17}$$

where

$$Z = 2\mu k^2(1 + ig)(\omega_1/\omega)^2, \quad \Omega_i = (\omega_i/\omega_1)^2,$$
$$A_{ij} = C_{Lij} - C_{Dij}, \quad A_{ii} = 2\mu k^2 + C_{Lii} - C_{Dii}. \tag{18}$$

4.4. Flutter Speed

Four U versus g curves were obtained by solving the flutter determinant for a number of reduced frequencies. Each curve corresponds to one eigenmode. The flutter speed is defined as the speed at which g first becomes zero in the U versus g curve. The dimensionless U versus g curves for three mass ratios ($\mu = 0{\cdot}1,\ 0{\cdot}39,\ 1{\cdot}0$) are shown in Figure 8. It was found that the U versus g curve for flutter are the fourth, third and second modes for $\mu = 0{\cdot}1,\ 0{\cdot}39,\ 1{\cdot}0$, respectively; the mode therefore becomes lower with increasing mass ratio. Hereafter, flutter in the nth mode is referred to as "nth mode flutter", and the mode that most influences flutter is referred to as the "primary mode".

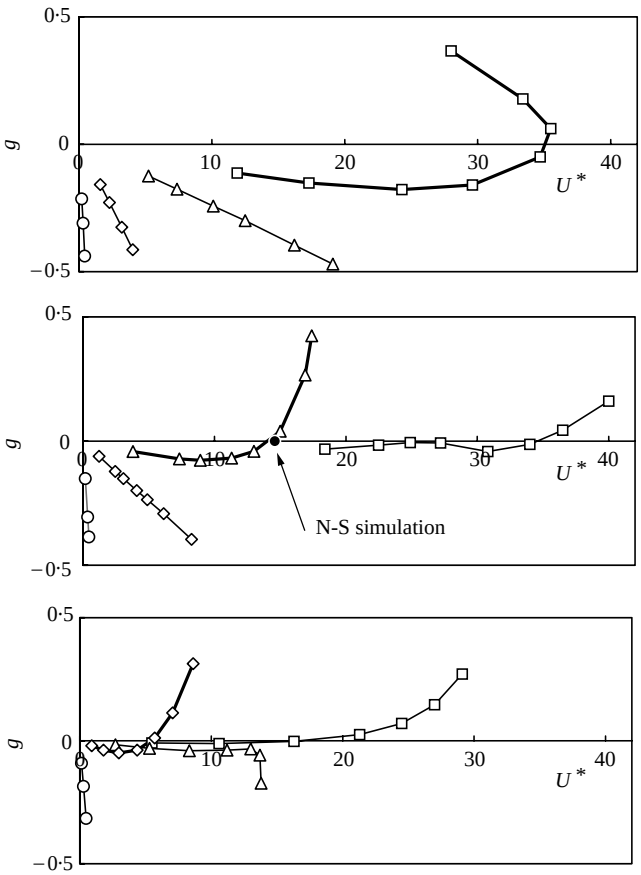

Figure 8. U versus g curve for: ○, first mode;◇, second mode; △, third mode; □, fourth mode. (a) $\mu = 0{\cdot}1$; (b) $\mu = 0{\cdot}39$; (c) $\mu = 1{\cdot}0$.

The flutter wind speeds obtained in the N–S simulation are also plotted and compared in Figure 8(b) ($\mu = 0{\cdot}39$). The flutter speeds calculated by these two methods are in good agreement. The computation time for potential flow analysis is very short, about 10 s per sheet using a personal computer (200 MHz Intel Pentium MMX Processor). The parametric study that follows was conducted using potential flow analysis.

Figure 9 shows the relationship between U_S^* and μ for the parametric and experimental analyses. Aerodynamic drag along the sheet surface was added to the potential flow analysis. The results for $C_D = 0{\cdot}0$, $0{\cdot}1$ and $0{\cdot}2$ are shown. According to Fairthorne (1930), the drag coefficient of flag paper is approximately $0{\cdot}1$ at $\mu = 0{\cdot}1$. Therefore, the $C_D = 0{\cdot}1$ results are considered to correspond to actual conditions. The range of primary flutter with $C_D = 0{\cdot}0$ and $0{\cdot}1$ is shown in the lower part of Figure 9. Qualitatively, U_S^* tends to decrease with increasing μ, which is in agreement with the experiment results. However, there is a considerable quantitative discrepancy between the results of the potential flow analysis and the experiment. The effect of C_D is not large enough to account for the magnitude of the discrepancy. Four mechanisms may be considered as contributing to this discrepancy: the effect of the aspect ratio of the sheet, span-wise deformation, stabilization due to deformation of the sheet surface by wind pressure, and the increase in the rigidity during paper flutter compared to the static value obtained in the tensile test and subsequently used in the formula for dimensionless flutter speed. The last mechanism was determined from observations in natural frequency tests using small sheets of paper in a vacuum vessel. However, the cause was not confirmed in the present study, and remains to be investigated.

The calculated solutions from the four potential theory approaches (methods 2, 5, 6, and 7) are compared in Figure 9. The solutions by methods 6 and 7 agree well in the range $0{\cdot}3 \leq \mu \leq 1$, and the solutions by methods 2, 5, and 7 agree well for $\mu > 1$. These results confirm the reliability of the method proposed in this study (method 7) over a wide range of mass ratio.

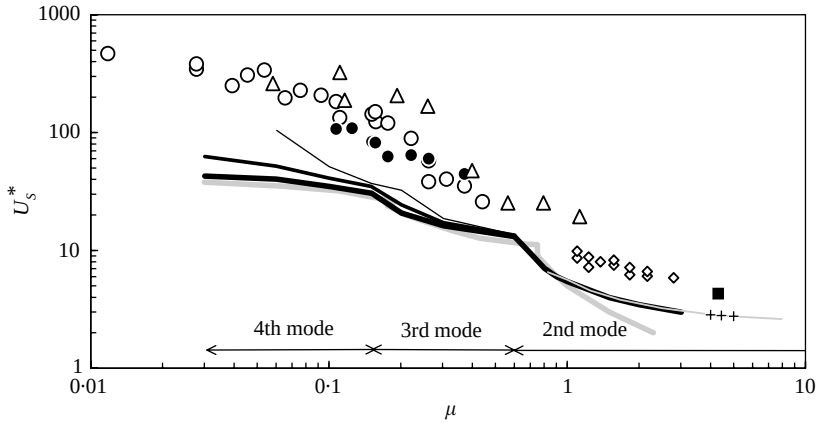

Figure 9. Relationship between dimensionless flutter speed and mass ratio. Present experiment: ○, flag-type paper; ●, long-type paper; △, elastic sheet; other experiment:◇, Huang (1995); ■, Kornecki *et al.* (1976). Present theory: very thick black line, $C_D = 0$; medium black line, $C_D = 0{\cdot}1$; ordinary line, $C_D = 0{\cdot}2$; other theories: +, Kornecki *et al.* (1976), —, Huang (1995); thick gray line, Guo & Païdoussis (2000).

4.5. Flutter Frequency

The relationship between dimensionless flutter frequency (F_f/F_1) and μ is shown in Figure 10, and the dimensionless natural frequencies of each primary mode ($F_4/F_1, F_3/F_1, F_2/F_1$) are shown by dotted lines in the same figure. The flutter frequency is the one to which the natural frequency changes by the effect of the unsteady lift as shown by arrows. Also there is a phenomenon in which the flutter frequency changes in step-like fashion at the transition point of the primary mode (near $\mu = 0{\cdot}15$ and $0{\cdot}7$).

4.6. Flutter Mode

The amplitude ratio and the phase of the four component modes versus mass ratio obtained from eigenvectors are shown in Figure 11. In this figure, $\sum \bar{q}_i^2 = 1$. Both the amplitude ratio and phase change significantly at the transition of the primary mode. The amplitudes below $\mu = 0{\cdot}7$ decrease in the order of first, second, third and fourth component. The amplitude of the fourth mode is negligible over $\mu = 0{\cdot}15$. When μ is greater than $0{\cdot}7$, the amplitudes of the modes higher than the second are negligibly small, and flutter can be approximated by two degrees of freedom: the first and second modes. The N–S simulation data at $\mu = 0{\cdot}39$ was obtained from Figure 2(a). Both analyses are in good agreement regarding the mode of flutter in that the amplitude ratio and phase of the components are consistent.

The motions of the flutter modes are constructed by substituting the amplitude ratio and phase of each mode into the following equation:

$$\bar{y}(x,\ t) = \sum_{i=1}^{4} \bar{q}_i f_i(x)\sin(\omega t + \phi_{i1}). \tag{19}$$

Figure 12 shows five mode-shapes that were generated from analysis data and one mode shape taken from the experiments. The amplitude of the analytical mode at $\mu = 0{\cdot}39$ was adjusted to that of the experimental mode. The amplitudes of the modes at other values of μ are shown at a similar scale, and as such differ from real amplitudes, which tend to

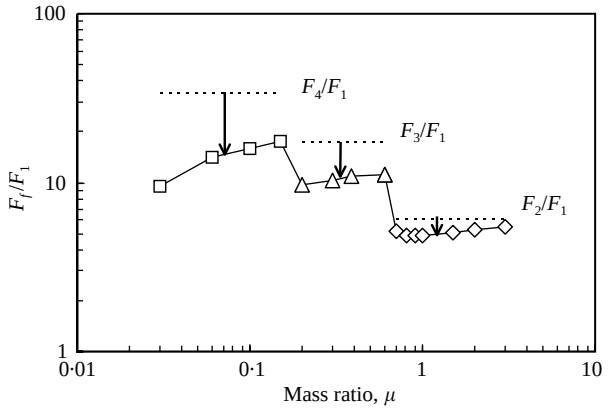

Figure 10. Relationship between dimensionless flutter frequency and mass ratio. F_f is the flutter frequency; F_i is the natural frequency of ith mode.

increase with increasing μ. The wavenumber was set at 10 for all analytical modes, which is not the same as in the experiment. The travelling wave motion is clearly observed at small values of μ; however, it approaches standing wave conditions with increasing μ.

5. MECHANISM OF FLUTTER GENERATION

The mechanism of flutter generation was investigated for second mode flutter by analysing the artificial damping g, which has been shown here to govern the flutter generation. According to Figure 11(a), the amplitudes of the third and fourth modes are so small that the equation for second mode flutter can be approximated by the equation with two degrees of freedom, involving the first and second modes alone, i.e.,

$$(Z - 2\mu k^2 - C_{L11})q_1 - C_{L12}q_2 = 0, \tag{20}$$

$$-C_{L21}q_1 + (F_2 Z - 2\mu k^2 - C_{L22})q_2 = 0. \tag{21}$$

Since it can be approximated as $Z = 0$ in equation (20) for the U versus g curve of the second mode, the following is obtained:

$$\frac{q_1}{q_2} = \frac{C_{L12}}{-2\mu k^2 - C_{L11}}. \tag{22}$$

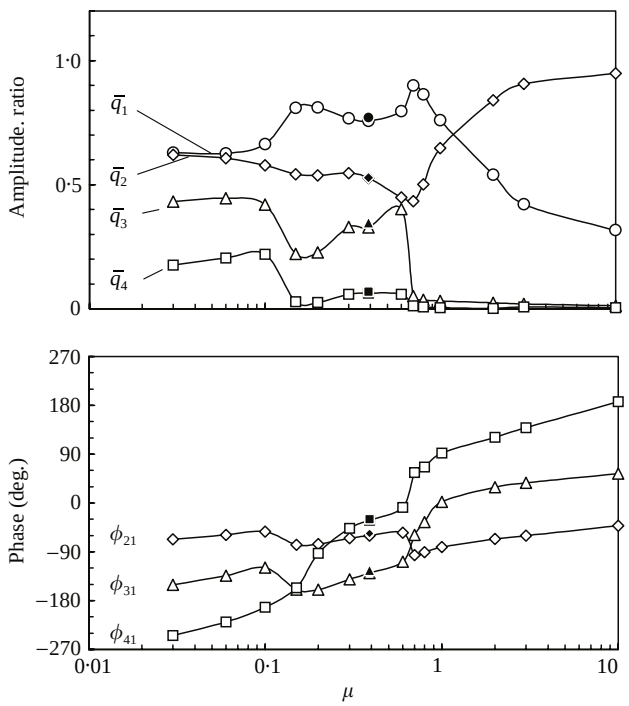

Figure 11. Amplitude ratio and phase of the four component modes versus mass ratio: ○, ◇, △, □ potential flow analysis ; ●, ◆, ▲, ■ N–S simulation. (a) Amplitude ratio of component mode, (b) phase between ith mode and first mode.

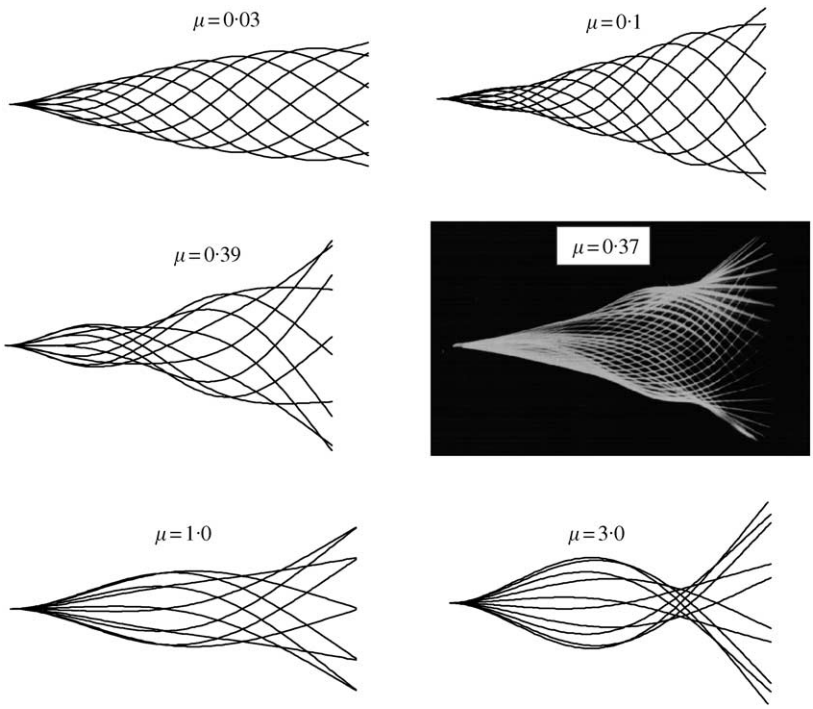

Fig. 12. Change of flutter mode due to mass ratio.

Assuming $q_2 = 1$, and by substituting equation (22) into (21), the following is obtained:

$$F_2 Z = (2\mu k^2 + C_{L22}) + C_{L21} q_1 \tag{23}$$

$$g = \mathscr{I}m(F_2 Z)/\mathscr{R}e(F_2 Z) \tag{24}$$

The first term on the right-hand side of equation (23) is the contribution of the second mode, and the second term is the contribution of the coupling term between the first and second modes.

The formation process of g in the unstable ($\mu = 1$, $k = 1$) is described as follows in reference to Figure 13: (i) the amplitude of the second mode (q_2) can be represented by a unit vector $(1, 0)$; (ii) the resultant force of inertia and unsteady lift for q_2 has a large real component and a small negative imaginary component; the effect of these mechanisms on flutter is therefore small; (iii) as follows from C_{L12} and the transfer function $[-1/(2\mu k^2 + C_{L11})]$, the amplitude of q_1 is amplified to about double that of q_2, and the phase of q_2 is advanced by about 90°; (iv) the second term on the right-hand side of equation (23) is located in the third quardrant, in which flutter is promoted; this is considered to be due to the fact that the coupling term $C_{L12}C_{L21}$ amplifies the transfer function $[-1/(2\mu k^2 + C_{L11})]$, as shown in expression H in Figure 13, which also causes a phase delay (β); therefore, the coupling term $C_{L12}C_{L21}$ can be considered to be the driving force for the flutter phenomenon; (v) the value of g becomes positive due to the effect of $C_{L12}C_{L21}$.

These results show that the coupling term $C_{L12}C_{L21}$ is the dominant factor in the second mode flutter. The authors have also confirmed that $C_{L23}C_{L32}$ and $C_{L34}C_{L43}$ are the

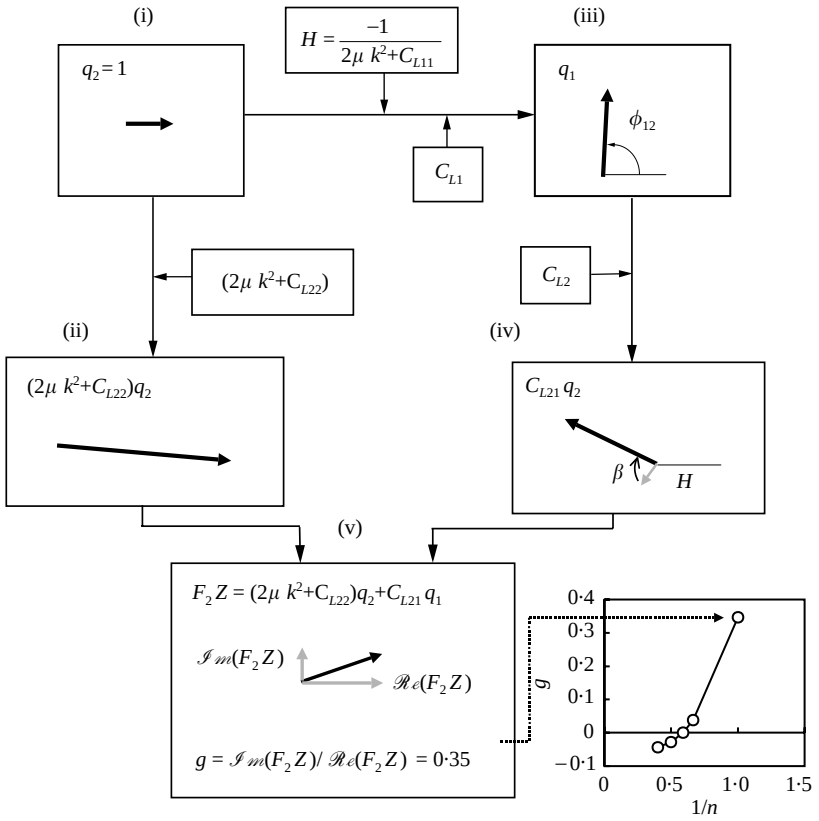

Figure 13. Formation process of artificial structural damping g in unstable condition.

dominant factors in the third and fourth mode flutter, respectively. Thus, it can be concluded that $C_{Ln-1,n}C_{Ln,n-1}$ is the dominant factor in the nth mode flutter.

6. CONCLUSION

Two different analytical methods were developed in order to investigate the phenomenon of paper flutter. The methods employed were N–S simulation using a super-computer, and potential flow analysis using a personal computer. The results are summarized as follows.

(i) In N–S simulation, the transient response and isovorticity contours were obtained by means of a time-marching scheme. It was shown that the flow around a fluttering sheet is similar to that obtained by potential flow analysis.

(ii) Potential flow analysis is adequate for parametric study, with a relatively short computation time of about 10 s per sheet using a personal computer yet providing the same accuracy as N–S simulation. A parametric study was carried out by potential flow analysis, and new phenomena that had not been recognized in experiments, such as the relationship between flutter mode and mass ratio, were discovered.

(iii) The formation process of g, which has been shown to govern the occurrence of flutter, was analysed in vector form, and the mechanism and dominant factor in flutter generation was clarified. It was shown that the coupling term in unsteady lift is the dominant factor in sheet flutter.

References

Bisplinghoff, R. L., Ashley, H. & Halfman, R. L. 1955 *Aeroelasticity*. Cambridge, MA: Addison-Wesley.

Fairthmore, R. A. 1930 Drag of flags. ARC R&M No. 1345.

Fung, Y. C. 1955 *An Introduction to the Theory of Aeroelasticity*. New York: John Wiley & Sons.

Guo, C. Q. & Païdoussis, M. P. 2000 Stability of rectangular plates with free side-edges in two-dimensional inviscid channel flow. *Journal of Applied Mechanics* **67,** 171–176.

Houbolt J. C. 1950 A recurrence matrix solution for the dynamic response of aircraft in gusts. NACA T.N. 2060.

Huang, L. 1995 Flutter of cantilevered plates in axial flow. *Journal of Fluids and Structures* **9,** 127–147.

Isogai, K. 1993 Numerical simulation of shock-stall flutter of an airfoil using the Navier–Stokes equations. *Journal of Fluids and Structures* **7,** 595–609.

Kornecki, A., Dowell, E. H. & O'Brien, J. 1976 On the aeroelastic stability of two-dimensional panels in uniform incompressible flow. *Journal of Sound and Vibration* **47,** 163–178.

Küssner, H. G. & Shwarz, I. 1941 The oscillating wing with aerodynamically balanced elevator. NACA Technical Memorandum 99.

Noguchi, H., Tanaka, H., Tanaka, K., Adachi, T. & Watanabe, Y. 1995 Application of vortex method to analysis of flag flutter. In *The 73rd JSME Fall Annual Meeting*, pp. 143–144. The Japan Society of Mechanical Engineers.

Watanabe, Y., Suzuki, S., Sueoka, Y. & Kunimaru, H. 1991 The flutter mechanism of sheet. In *Proceedings of the First International Conference on Web Handling*, Oklahoma State University, Stillwater, OK, USA, pp. 246–256.

Watanabe, Y., Isogai, K., Suzuki, S. & Sugihara, M. 1997 Analysis of paper sheet flutter. In *Proceedings of Second International Conference on Flow Interaction cum Exhibition/Lectures on Interaction of Science & Art*, Berlin, pp. 45–47.

Watanabe, Y., Suzuki, S., Sugihara, M. & Sueoka, Y. 2002 Experimental study of paper flutter. *Journal of Fluids and Structures* **16,** 529–542.

Yamaguchi, N., Yokota, K. & Tsujimoto, R. 1999 Fluttering behavior of a flexible thin sheet in high-speed flow. (1) Theoretical method for prediction of the sheet behavior for small perturbed theory. *Nihon Kikai Gakkai Ronbunshu* **65,** No. 632, pp. 1224–1231.

Yee, H. C. & Harten, A. 1985 Implicit scheme for hyperbolic conservation laws in curvilinear coordinates. AIAA Paper 85–1513.

APPENDIX: NOMENCLATURE

A	area of one side of the sheet surface
b	semichord
c	chord length
c_p	unsteady pressure coefficient, $p/(\frac{1}{2}\rho U^2 q/b)$
C_{Lij}	generalized unsteady lift coefficient, $Q_{Lij}/(\frac{1}{2}\rho U^2 q_{j\varphi})$
C_{Dij}	generalized drag coefficient, $Q_{Dij}/(\frac{1}{2}\rho U^2 q_j)$
C_D	drag coefficient, $T/(\frac{1}{2}\rho U^2 A)$
d	web span
EI	bending stiffness per unit width
f_i	ith natural mode function
F	frequency

F_f	flutter frequency
F_i	natural frequency of ith natural mode
g	artificial damping coefficient in $U-g$ method
h	thickness of sheet
i	imaginary unit, $\sqrt{-1}$
k	reduced frequency, $b\omega/U$
m	area density of sheet, $\rho_p h$
M_i	generalized mass
p	unsteady pressure
q	generalized coordinate
q^*	dimensionless generalized coordinate, q/b
Q_L	generalized lift force
Q_D	generalized drag force
t	time
t^*	dimensionless time, $(U/b)t$
T	tension
U	flow speed
U_S	sheet flutter speed (self-excited starting point)
U_Q	sheet flutter speed (quenching point)
U^*	dimensionless flow speed
U_S^*	dimensionless sheet flutter speed (self-excited starting point)
x, y	Cartesian coordinates
x^*, y^*	dimensionless Cartesian coordinates, x/b, y/b
Greek letters	
μ	mass ratio, $m/\rho c$
ρ	air density
ρ_p	density of sheet material
ϕ_{ij}	phase between ith mode and jth mode
ω	circular frequency
θ	$-\cos^{-1}(x/b)$